PNAS RESEARCH ARTICLE | APPLIED PHYSICAL SCIENCES

Terrestrial locomotion of microscopic robots enabled by 3D nanomembranes with nonreciprocal shape morphing

Yang Wang[a,b], Xing Li[a,b], Chang Liu[a,b], Yunqi Wang[a,b], Chunyu You[a,b], Hong Zhu[a], Zhi Zheng[a,b], Ziyu Zhang[a,b], Guobang Jiang[a,b], Xiang Dong[a,b], Tianjun Cai[a,b], Ziao Tian[c], Zengfeng Di[c], Gaoshan Huang[a,b], Xiangzhong Chen[a,b,d], Enming Song[a,d], Jizhai Cui[a,b,1], and Yongfeng Mei[a,b,d,1]

Affiliations are included on p. 10.

Edited by John Rogers, Northwestern University - Evanston, Evanston, IL; received January 10, 2025; accepted May 19, 2025

Microscopic robots exhibit efficient locomotion in liquids by leveraging fluid dynamics and chemical reactions to generate force asymmetry, thereby enabling critical applications in photonics and biomedicine. However, achieving controllable locomotion of such robots on terrestrial surfaces remains challenging because fluctuating adhesion on nonideal surfaces disrupts the necessary asymmetry for propulsion. Here, we present a microscopic robot composed of three-dimensional nanomembranes, which navigate diverse terrestrial surfaces with omnidirectional motion. We propose a general mechanism employing nonreciprocal shape morphing to generate stable asymmetric forces on surfaces. This nonreciprocal shape morphing is realized through a laser-actuated vanadium dioxide nanomembrane, leveraging the material's inherent hysteresis properties. We demonstrate that these robots can be fabricated in various shapes, ranging from simple square structures to bioinspired "bipedal" helical designs, enabling them to directionally navigate challenging surfaces such as paper, leaves, sand, and vertical walls. Furthermore, their omnidirectional motion facilitates applications in microassembly and microelectronic circuit integration. Additionally, we developed an artificial intelligence control algorithm based on reinforcement learning, enabling these robots to autonomously follow complex trajectories, such as tracing the phrase "hello world". Our study lays a theoretical and technological foundation for microscopic robots with terrestrial locomotion and paves a way for microscopic robots capable of operating on surfaces for advanced nanophotonic, microelectronic, and biomedical applications.

microrobots' locomotion | three-dimensional nanomembranes | shape morphing | vanadium dioxide | nonreciprocal

Significance

Microscopic robots are of practical interest in photonics and biomedicine, relying on efficient, directional locomotion in various environments. However, achieving such locomotion in terrestrial environments remains challenging because fluctuating adhesion disrupts the necessary force asymmetries. This work presents a general locomotion mechanism that enables microscopic robots to navigate diverse terrestrial environments. The mechanism relies on nonreciprocal shape morphing to generate force asymmetry, achieved by laser-actuated three-dimensional vanadium dioxide nanomembranes. The nanomembrane-based microscopic robots can be fabricated on demand, navigate surfaces like paper and leaves omnidirectionally, be applicable in microassembly and microelectronics, and move autonomously under an AI algorithm control. These findings demonstrate a theoretical and technological foundation for microscopic robots operating in terrestrial scenarios, with potential in advanced interdisciplinary applications.

Locomotion is a fundamental capability for both robots and organisms (1–4), which requires the generation of asymmetric forces that interact with the local environment (5–8). At the microscopic scale, many natural microscopic organisms live in fluidic environments and achieve directional locomotion by generating asymmetric forces through periodic deformations (e.g., the beating of hair-like flagella for propelling) (9). This is because in microscale fluid environments with a low Reynold number, viscous forces dominate, making nonreciprocal deformations effective for generating asymmetry (10). Moreover, the continuity of fluids enables stable chemical gradients that contribute to force asymmetry (11). Inspired by these mechanisms, significant efforts have been made to develop artificial microscopic robots in fluid environments (12–20), which are smaller than the resolution limit of human vision (less than a hundred micrometers) and demonstrate efficient locomotion. These robots have shown great promise in applications such as nanophotonics (13, 17), drug delivery (14, 19, 20), and nanotheranostics (21). However, in terrestrial environments dominated by fluctuating surface forces (22–26), developing microscopic robots capable of directional locomotion remains challenging due to the difficulty in overcoming friction (27–30) and generating stable asymmetric forces (28, 29).

Recent breakthroughs in materials design (27–31) have enabled microscopic robots to generate high actuation forces, allowing them to overcome surface friction. These efforts mainly follow two approaches: One relies on soft materials with dramatic contraction under stimuli, such as light-driven liquid crystal elastomers (28), and the other leverages high-frequency pulsed lasers to produce impulsive excitation in materials like metal nanostructures (27, 29) and 2D materials (30). Nevertheless, they remain susceptible to fluctuating surface friction forces (28, 32), restricting their movement to specialized or ideal surfaces. Developing microscopic robots that can achieve omnidirectional locomotion on diverse terrestrial surfaces remains a highly sought-after goal, offering broader applications for artificial micromachines (13, 17, 33).

This article is a PNAS Direct Submission.

[1]To whom correspondence may be addressed. Email: jzcui@fudan.edu.cn or yfm@fudan.edu.cn.

This article contains supporting information online at https://www.pnas.org/lookup/suppl/doi:10.1073/pnas.2500680122/-/DCSupplemental.

Published June 17, 2025.

Here, we present a microscopic terrestrial robot, capable of effective locomotion by leveraging asymmetric friction forces through a sequence of nonreciprocal shape morphing within a three-dimensional (3D) nanomembrane. A general model is first developed to predict the robot's motion with different shape-morphing strategies. Based on this model, we establish the theory that for a microscopic robot, locomotion based on reciprocal deformation is highly influenced by fluctuating surface friction, leading to random motion (Fig. 1 *A*, *Left*). In contrast, when the robot undergoes our proposed nonreciprocal deformation, it alternately increases the contact areas of different legs, creating stable friction asymmetry that is independent of the surface structure (Fig. 1 *A*, *Right*). As a result, the microscopic robot achieves controlled directional motions. To realize such a microscopic robot with nonreciprocal deformation, we used a focused laser beam to actuate 3D vanadium dioxide (VO_2) nanomembranes. VO_2 is a Mott phase transition material (34) that exhibits strain–temperature hysteresis, with a compressive strain up to 0.45% (Fig. 1 *B*,

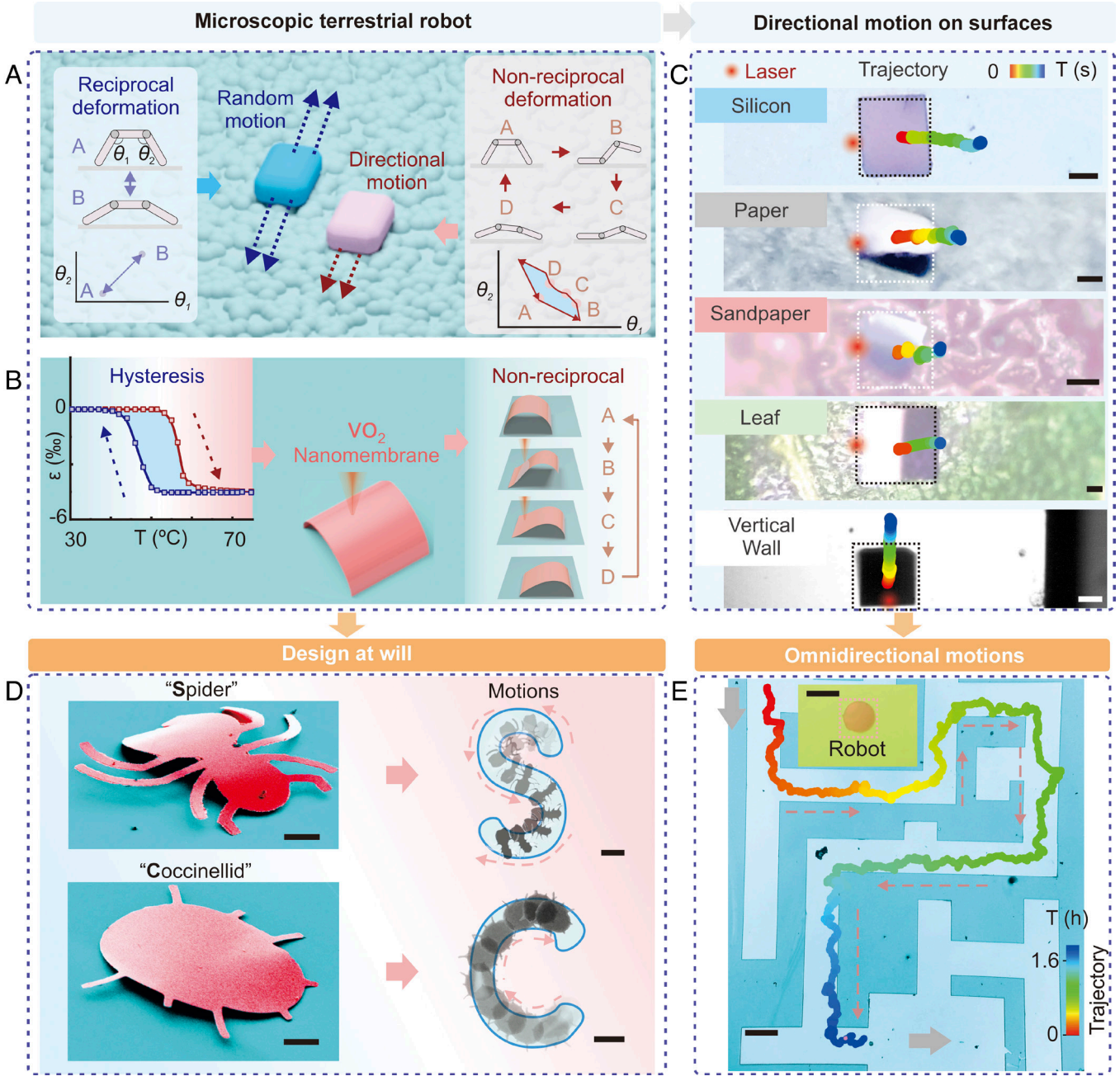

Fig. 1. Schematics of microscopic robots on terrestrial surfaces enabled by vanadium dioxide (VO_2) nanomembranes with nonreciprocal shape morphing. (*A*) Microscopic robots achieving motions on terrestrial surfaces with different deformation. (*B*) The diagram for realizing directional motions of microscopic robots using VO_2 nanomembranes. *Left*, Strain changes in VO_2 with hysteresis loop (blue area) during heating–cooling cycles. *Middle*, Diagram of the 3D VO_2 nanomembrane robot. *Right*, Schematic illustration of controllable nonreciprocal deformation design. (*C*) Terrestrial locomotion of microscopic robots (dimensions: 50 μm × 50 μm × 180 nm) actuated by a pulsed laser at different frequencies (f) and time (T). The robots move on silicon (f = 20 Hz, T = 35 s), paper, (f = 20 Hz, T = 105 s), sandpaper (f = 100 Hz, T = 45 s), leaf (f = 100 Hz, T = 35 s), and vertical walls (f = 5 Hz, T = 8 s). (*D*) Custom-designed microscopic robots. *Left*: Scanning electron microscope (SEM) images of microrobots shaped as a "spider" and a "coccinellid." *Right*: Motion trajectories of the spider and coccinellid robots, with earlier positions indicated by more transparent images. (*E*) Omnidirectional locomotion of microscopic robots. Circular robots navigated a large maze by traveling along *Top*, *Bottom*, *Left*, and *Right* directions over a total distance of 1 cm, continuously operating for 1.6 h. [Scale bars, 25 μm (*C*), 20 μm (*D* SEM), 100 μm (*D* trajectory), 35 μm (*E Inset*), 300 μm (*E*)].

Left). This strain induces large output force (35), making it possible for terrestrial microscopic robots to overcome friction. Moreover, due to the ultralow bending stiffness of 3D nanomembranes, the phase transition–induced strain results in out-of-plane deformation, which can be used as a platform for generating nonreciprocal shape morphing (Fig. 1*B*, *Right*). Therefore, using laser actuation, the microscopic robot based on 3D nanomembranes can navigate diverse surfaces with directional motions. For example, VO_2 microscopic robots with square-shapes can move directionally on silicon, oxides and metals surface—materials commonly used in laboratory settings. These square-shaped robots can also move directionally on the papers, sandpapers, sands, leaves and foils surfaces, which are more representative of real-world environments. Furthermore, these robots are capable of climbing vertical walls in a controlled direction, unaffected by gravity (see all motions in Fig. 1*C* and *SI Appendix,* Fig. S1 and Movie S1).

Moreover, since the directional motion of microscopic robots only requires adherence to our proposed mechanism, the shape of robots and direction of motions can be designed at will. The shape of the robots is customizable, thanks to our CMOS-compatible fabrication process of 3D nanomembranes. For example, robots shaped like spiders and coccinellids can trace trajectories directionally of the letters "S" and "C" under laser control (Fig. 1*D* and Movie S2). Moreover, we demonstrate a circular microscopic robot can navigate omnidirectionally, moving over 1 cm in a maze, highlighting the robustness and controllability of this approach under fluctuating frictional conditions on surfaces (Fig. 1*E* and Movie S3).

Results

Concept and Design of Terrestrial Locomotion of Microscopic Robots. Terrestrial locomotion requires effective friction modulation, aiming to create asymmetric forces when interacting with the ground surface. According to Coulomb's model, dry friction is $f = \mu N$, where μ is the coefficient of friction and N is the normal force (5). When organisms move at the macroscopic scale, such as human walking at the meter scale, inchworms wriggling at the centimeter scale, and *Dicopomorpha echmepterygis* [the smallest known insect (36)) crawling at the submillimeter scale, the normal force mostly counteracts gravity. So friction is $f = \mu mg$ with relations $f \propto L^3$, where mg and L are gravity and feature size, respectively *(SI Appendix,* Fig. S2*)*. For effective locomotion at this scale, based on periodic changes in body shape, organisms and robots either change the location of their center of mass to modulate the normal force (4, 7, 8, 37) N or use anisotropic structures to modulate the friction coefficient μ (1, 6), resulting in asymmetric friction forces. For microscopic objects with feature size L<100 μm that are invisible by the naked eye (15, 33), gravity is much smaller, and the normal force acts mostly to counterbalance surface adhesion (22). Therefore, the friction is $f = \mu N_{adhesion}$ with relations $f \propto L$ (*SI Appendix*, note 1). At this scale, surface inhomogeneities and charge differences induce the variation of both the friction coefficient and the surface adhesion, resulting in fluctuating friction forces (25). Under such fluctuations, asymmetric frictions are difficult to generate (38), which is probably one of the reasons why no freely moving creatures on dry surfaces are found at this scale (28). We measured the friction on a 0.2 μm × 1 μm region of a silicon surface using lateral force microscopy (Fig. 2*A*). Clear difference in friction was found not only at different locations but also at the same location when scanned along different directions (f_+ scanned from "−" to "+", f_- scanned from "+" to "−", Fig. 2*B*). For real-world terrestrial surfaces, such as paper and leaves, the fluctuations in friction, which is proportional to surface roughness, would be much more significant (*SI Appendix,* Fig. S3) (24, 25).

Under such surface conditions, we simulate the trajectory of a microscopic robot locomoting with periodic shape changes (*SI Appendix*, Microrobot trajectory simulation), as shown in Fig. 2*C*. Here, a three-link model with two degrees of freedom is used, whose deformation is determined by the two joint angles (θ_1, θ_2). When the robot goes through a sequence of reciprocal shape morphing (Fig. 2 *C, i*), the robot changes to a certain shape and then returns to the original shape by going through the sequence in reverse, defining an open curve (A-B-A) in the configuration space of (θ_1, θ_2) (10) (*SI Appendix,* Fig. *S4*). With this reciprocal deformation, the asymmetric sliding frictions at the front leg and back leg (f_- or f_+ depending on the moving direction) are completely determined by the situation of the surface, so that when starting from three different points I, II, and III, the microscopic robots all move in the direction with lower friction in their local environment ($f_- < f_+$ for point I, $f_- > f_+$ for points II and III, quasi-static analysis in *SI Appendix,* Fig. *S4 A–C*), and stop at the point where the local friction gradient is disrupted *(SI Appendix*, note 2 and Figs. S5–S7*)*. This corresponds to the robots displaying "random walk" behavior in the reported work (28, 32). Previous attempts for deterministic motion control primarily focused on engineering the surface, such as using periodic grating surfaces (28) or ultraflat surfaces with lower friction fluctuation (27, 29–31). On real-world surfaces where the fluctuating friction cannot be eliminated (26), developing strategies for microscopic robots to move freely remains challenging.

We propose a nonreciprocal shape change sequence that can generate asymmetric forces on the legs, as an effective way of microscopic terrestrial locomotion. When the structure goes through nonreciprocal shape morphing, the robot changes to a certain shape and then returns to the original shape by going through a different sequence, showing a closed loop in the configuration space (A-D-C-B-A), as shown in Fig. 2 *C, ii* (10). In this deformation sequence, at the A and C states, the sliding frictions at the front leg and back leg increase by N times (assuming the contact areas, and therefore the adhesion forces, increase by N times), and friction asymmetry $Nf_- > f_+$ can be maintained no matter what the relationship between the magnitudes of surface frictions f_- and f_+ is, as long as N is sufficiently large. In this case, the frictions on the robot are actively regulated, and the robot can move deterministically in the "+" direction regardless of the fluctuating surface friction and therefore unrelated to the surface situation *(SI Appendix,* Fig. *S4 D–F)*. Similarly, utilizing a reverse sequence (A-B-C-D-A), at the states A and C, $f_- < Nf_+$ can be maintained as shown in Fig. 2 *C, iii*, and the microscopic robot can move in the "-" direction in a controlled manner *(SI Appendix,* Fig. *S4 G–I)*. The strategy is adaptable from one-dimensional systems to complex two-dimensional (2D) structures, suitable for various deformation modes such as stretching and bending (*SI Appendix*, Note 2 and Figs. S8–S10).

To achieve nonreciprocal shape morphing at the microscopic scale, we developed a 3D nanomembrane structure composed of VO_2, which offers multiple degrees of freedom for deformation. The fabrication process for these 3D VO_2 microstructures is illustrated in Fig. 2*D* (see Details in *SI Appendix*, *Methods Sample Fabrication* and Figs. S11 and S12). A 180 nm thick polycrystalline VO_2 thin film was deposited on the SiO_2/Si substrates (Fig. 2*E*) using magnetron sputtering (*SI Appendix*, note 3 and Figs. S13–S18) and subsequently patterned via photolithography. The patterns were then released by wet etching. By employing strain-engineering (39, 40) techniques (*SI Appendix*, note 4 and Figs. S19–S21), the VO_2 thin films can roll up and transform into

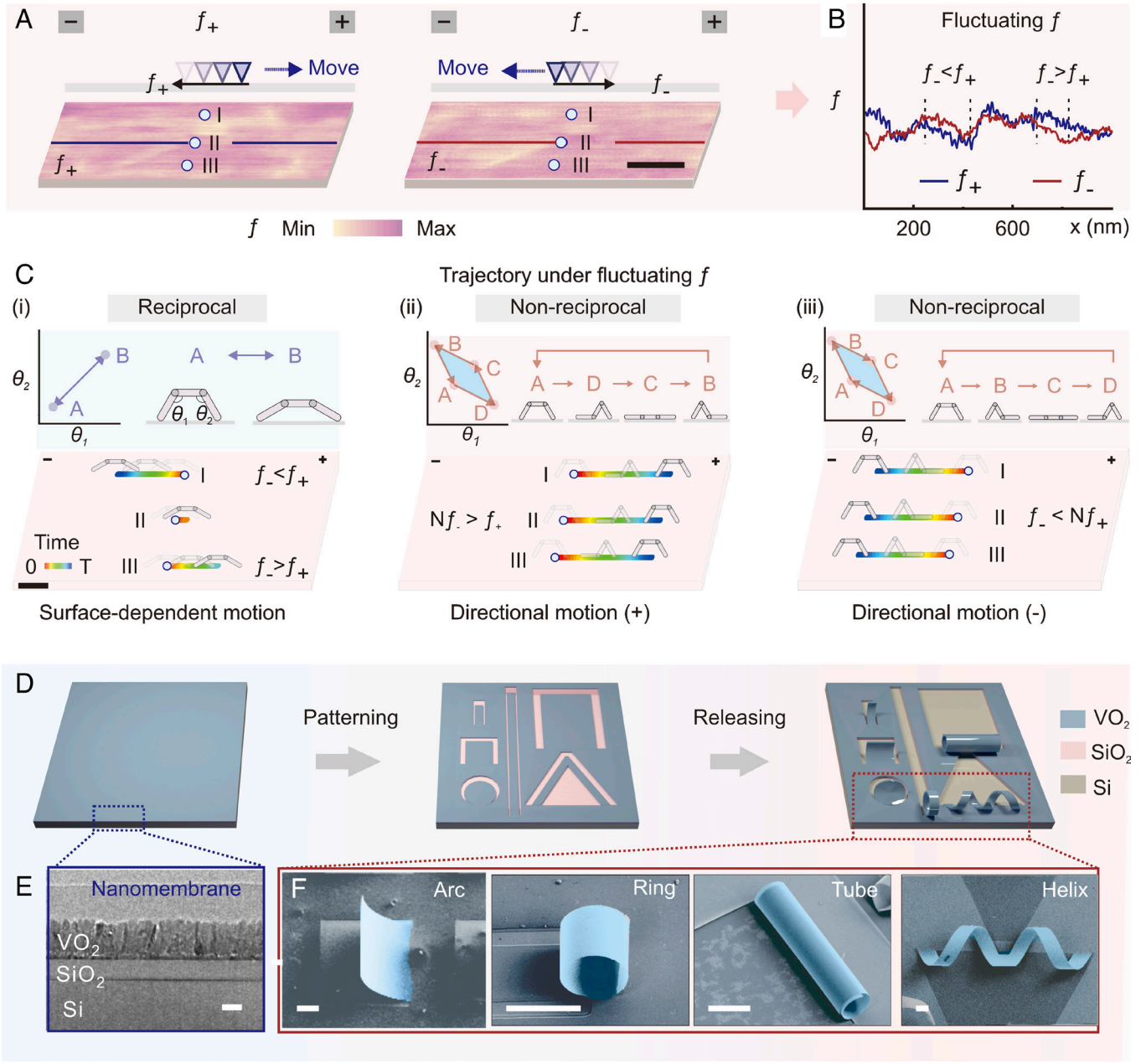

Fig. 2. Design of a nonreciprocal shape-morphing strategy for microscopic terrestrial locomotion. (*A*) Frictional forces experienced by a tip moving in opposite directions on a silicon wafer (dimensions: 0.2 μm × 1 μm). The tip moving from negative (positive) to positive (negative) suffers f_+ (f_-) friction. (*B*) Frictional values measured when the tip moves along the line passing through point II. (*C*) Schematics of shape-morphing strategies: (*i*) reciprocal shape morphing; (*ii*) nonreciprocal shape morphing following the sequence A-D-C-B-A, and (*iii*) nonreciprocal shape morphing following the sequence A-B-C-D-A. For each strategy, the *Top* row shows the structure during shape-morphing sequences, and the *Bottom* row presents simulated trajectory under fluctuating friction conditions. Starting points I, II, and III are highlighted in panel (*A*). (*D*) Fabrication progress of three-dimensional (3D) VO_2 nanomembranes for microscopic robots. (*E*) Cross-sectional high-resolution transmission electron microscopy (TEM) images of VO_2 nanomembrane on substrates. (*F*) Rolled-up 3D VO_2 nanomembranes with various shapes, including arcs, ring, tube, and helix. [Scale bars: 200 nm (*A*), 100 nm (*C*), 100 nm (*E*), 20 μm (*F*, SEM)].

freestanding 3D microstructures. Furthermore, by tailoring the planer shapes, a variety of rolled-up microstructures—including arcs, rings, tubes, and helices (Fig. 2*F*)—can be fabricated on demand (*SI Appendix*, note 5 and Figs. S22–S25), broadening their applicability to diverse structures and surfaces.

Nonreciprocal Shape Morphing in VO_2-Based Microstructures for Robots. The generation of nonreciprocal shape changes in VO_2 microstructures is systematically investigated. In order to obtain sufficiently large and therefore observable deformation, we fabricated 3D ring structures with one end free and the other end fixed to the substrate (Fig. 3*A*). Under laser irradiation, the photothermal effect induces the phase transition of VO_2 when heated above 325 K, which produces a compressive strain gradient (about 0.11%, *SI Appendix*, note 6(*i*) and Figs. S26–S28) that unrolls the microstructure. When the laser is off, the structure cools down and returns to its original state. Such actuation performance can be maintained during million times of laser on–off cycles with appropriate laser power density (*SI Appendix*, Fig. S29). To quantify the deformation actuated by the laser, the position of the tip, which is the free end of the ring structure (Fig. 3*B*), is tracked in a side view using an optical microscope (*SI Appendix*, *Tracking microstructure tips*). We observe that when the laser is on, the tip follows a path that is different from the path when the laser is off.

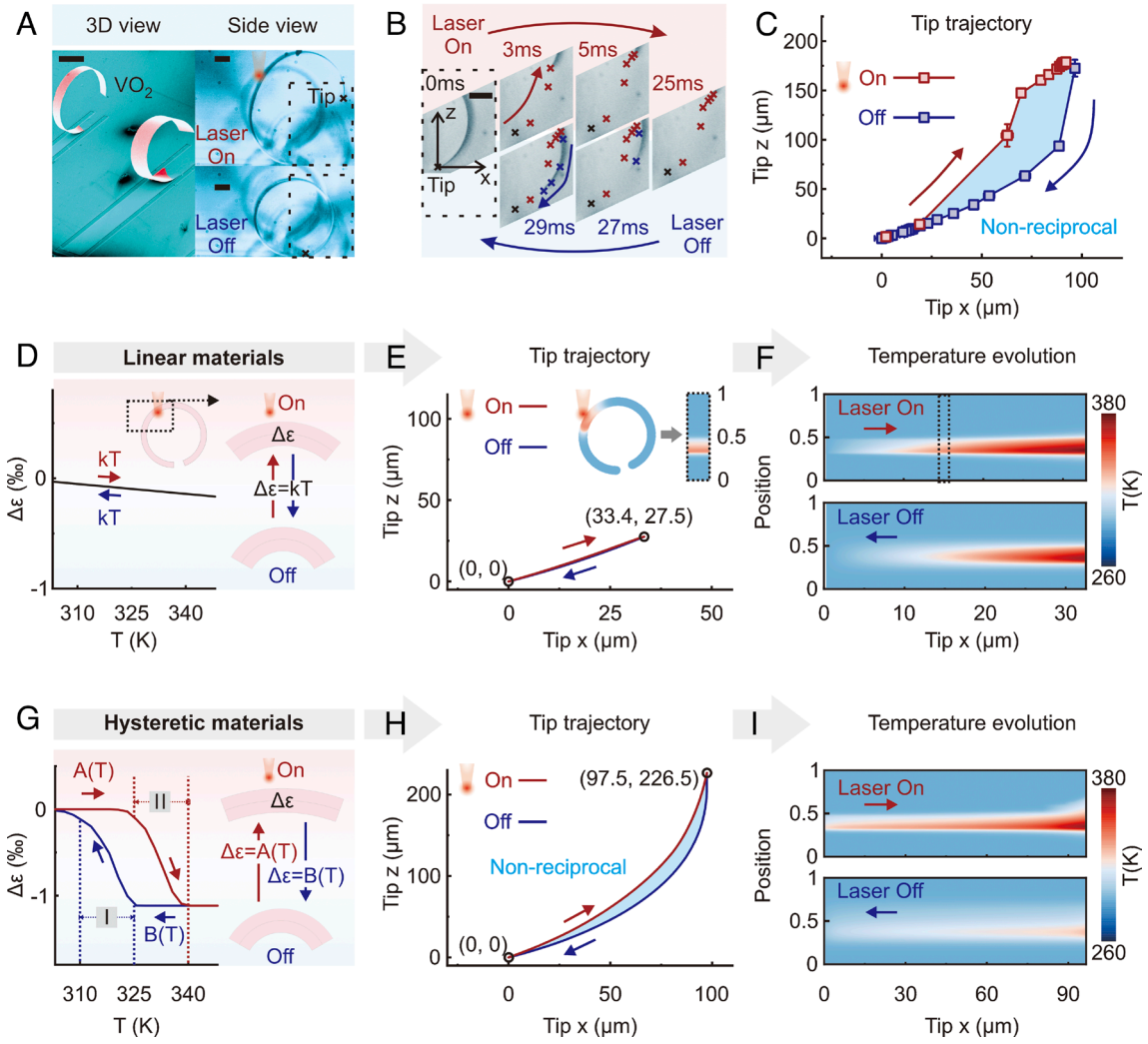

Fig. 3. Experimental analysis and numerical simulation of nonreciprocal shape morphing in VO_2-based microrobots. (*A*) SEM image of VO_2 ring-shaped microstructures (*Left*) and side view photos of the ring structure when the laser is on and off (*Right*). The laser position is depicted by a red symbol, and the tip is highlighted as an "X" mark. (*B*) The tip trajectory of the ring structure during a laser pulse actuation (square wave, 20 Hz frequency). Tip positions at certain times during the laser on and off are marked as red and blue X, respectively. (*C*) Analysis of tip trajectories under successive laser pulses. *D*–*I*, Simulation of tip trajectories of ring structure implemented with linear (*D*–*F*) and hysteretic materials (*G*–*I*). (*D* and *G*) The relationship between strain and temperature of linear materials (*D*) and hysteretic materials (*G*). The insets show schematics of the structure changing during the laser on and off. (*E* and *H*) Simulated tip trajectory with linear (*E*) and hysteretic materials (*H*). Insets in (*E*) show the temperature distribution on the ring when the laser is turned on and the displacement of the tip along the *x*-axis is 15 μm. (*F* and *I*) Temperature evolution of ring structure when the laser is on and off. The horizontal coordinate uses the displacement of the tip along the *x* axis during actuation. [Scale bars: 50 μm (*A*, *Left*), 50 μm (*A*, *Right*), 50 μm (*B*)].

Therefore, during a full on–off cycle, the tip trajectory goes around a closed loop, representing the nonreciprocal shape changes of the VO_2 microstructure (Fig. 3*C* and Movie S4). By altering the parameters for actuation (such as irradiation frequency, power, and position) and the geometric design of the microstructure, various close-loop trajectories can be achieved (*SI Appendix*, note 7 and Figs. S30–S33) which opens up a large design space for the nonreciprocal shape morphing.

Further, multiphysics simulations are implemented to study the mechanism of the nonreciprocal deformation in VO_2 microstructures (details in *SI Appendix*, *Simulation of microrobots shape morphing* and Fig. S34). We compare the shape change of the microstructures made by linear materials (coefficient of thermal expansion (CTE) independent of temperature T, showing a linear T-ϵ relation) and hysteretic materials [CTE depending on temperature, showing a nonlinear T-ϵ hysteresis (41). We use a double-layer model for the strain gradient that causes the shape change during the laser irradiation [*SI Appendix*, note 6(*ii*)], which is expressed as $\Delta\epsilon = kT$ (k: the difference in the CTEs between the two layers). First, two linear materials with different CTEs are used. Since their CTEs are constant during the temperature change, $\Delta\epsilon$ and T have the same relationship during heating and cooling (Fig. 3*D*). With this, we simulate the laser-induced deformation and track the tip position. The tip trajectory from (0, 0) to (33.4, 27.5) when the laser is on has minimal difference to the trajectory back to (0, 0) when the laser is off (Fig. 3*E*). This means the shape changes closely match during the heating and cooling processes. The tip trajectory during a full heating–cooling cycle is therefore very close to an open curve, representing an approximate sequence of reciprocal shape changes. Since this deformation results from thermal expansion, we study the temperature distribution on the ring structure during the deformation. When the laser is on, the tip moves in the *x* direction from 0 to 33.4 μm and the temperature at the irradiated region gradually increases to above 300 K (Fig. 3*F* top panel); when the laser is off, the tip moves back from 33.4 to 0 μm and the structure gradually cools down to room temperature (Fig. 3*F* bottom panel). There is only a slight difference in the temperature distribution (probably

because heating is localized at the irradiated position when the laser is on and spread out through the device when the laser is off[31]); therefore, the shape changes and the tip trajectories during the laser on and off processes closely resemble each other.

For comparison, materials with different hysteresis loops are utilized in the double-layer model for the strain gradient [here using two types of VO_2 with different hysteresis regulated by residual stress (42), *SI Appendix*, note 6(*iii*)]. The strain gradient $\Delta\varepsilon$ is expressed as two separate functions, i.e. *A(T)* for heating and *B(T)* for cooling, showing a hysteresis during the heating–cooling cycle (Fig. 3*G*). We simulate the deformation of the ring structure (*SI Appendix*, note 8 and Figs. S35–S37), and the tip moves from (0, 0) to (97.5, 226.5) and back during a full laser on–off cycle, as shown in Fig. 3*H*. Here, the tip displaces much further (due to a larger $\Delta\varepsilon$) than the tip of the ring structures made by linear materials. Besides, the tip trajectories during the laser on and off exhibit clear disparities, meaning the shape changes during these two processes differ significantly from one another. The full trajectory goes around a closed loop, which represent a sequence of nonreciprocal shape changes (Movie S5). We study the temperature distribution during the deformation, which are shown in Fig. 3*I* top and bottom panels for laser on and off processes, respectively. Compared to Fig. 3*F*, larger heat zones result from changes in relative positions of the laser irradiated on the ring because of the large deformation (43, 44). Here, the temperature evolutions show a significant difference between processes with the laser on and off. This is because the thermal-induced change of the strain gradient obeys different functions, which are *A(T)* and *B(T)* during heating and cooling (Fig. 3*G*), respectively. Specifically, during heating when considering the function *A(T)*, the strain remains relatively stable along with temperature changes in region I (T = 310 to 325 K) and undergoes rapid changes in region II (T = 325 to 340 K). Conversely, during cooling with the function B*(T)* applied, the strain maintains stability in region II and experiences rapid changes in region I. Therefore, during heating the ring structure remains barely deformed below 325 K, and the shape change mostly occurs during region II between 325 K and 340 K; during cooling the structure undergoes minimal deformation until 325 K, while most shape change during region I between 310 K to 325 K. The different temperature–strain relations *A(T)* and *B(T)* induce drastically different temperature distributions, therefore the tip goes through different paths during heating and cooling, representing a sequence of nonreciprocal shape changes in a full on–off cycle of the laser. We also consider using phase change materials without the hysteresis (i.e., $\varepsilon = A(T)$ for both heating and cooling, *SI Appendix,* Fig. *S38 A–C*), finding the tip trajectory showing only slight nonreciprocity. Moreover, the curvature distributions of structures with hysteretic, linear, and phase change materials are calculated according to temperature–strain relations and bending theories (*SI Appendix*, note 6), showing similar results as temperature distributions *(SI Appendix,* Fig. *S38 D–F)*. Hence, out of the three materials compared, hysteric materials have the largest difference in temperature distribution, curvature distribution, and tip paths during heating and cooling, showing that the hysteretic material property plays a vital role for the generation of nonreciprocal shape changes.

Directional Locomotion of Microscopic Robots with Nonreciprocal Deformation. Based on the VO_2 with nonreciprocal shape changes induced by laser irradiation, we fabricate simple microscopic robots achieving effective locomotion. First, we refer to the three-link model with the nonreciprocal deformation sequence (Fig. 4 *A Top* panel) proposed in *SI Appendix*, note 2, while the contact areas, and therefore the frictions at the front end and back end, increase alternately. By tracing the front end (highlighted by a red dot) in a side view in *(x, z)* coordinates, we obtain a 2D trajectory (Fig. 4*B*) where the paths are different when the laser is turned on and off, and this signature open-ended trajectory represents the effective displacement of the robots. Microscopic ring structures detached from the substrates, modeled by finite element methods (FEM), demonstrate very similar nonreciprocal shape changes and therefore effective displacement when actuated by the focused laser (Fig. 4*A* middle). At first, both ends of the ring are in contact with the ground. When the laser is on, the contact area at the back end increases, causing the front end to lift off the ground and extend forward (*Insets* in Fig. 4 *A Middle* panel). When the laser is off, the front end reestablishes contact with the ground, now with an increased contact area, while the contact area at the back end decreases. With this sequence of nonreciprocal shape changes, we observe an open-ended trajectory of the front end (Fig. 4*C*) similar to Fig. 4*B*, representing the effective terrestrial locomotion of the ring structure.

Similar effective locomotion realized by nonreciprocal shape changes induced by focused laser is observed in experiments, such as the alternative increase/decrease of the contact areas at the front and back ends (Fig. 4 *A Bottom* panel) and the open-ended trajectories (Fig. 4*D* and Movie S6). We further studied VO_2 microscopic robots in various shapes, such as arcs, helices, and tubes (Movie S7). We show a square-shaped arc structure, where the top view and side view of the robot is shown in Fig. 4*E*. When tracking two corners of the plate in a side view (point A, B), the distinct open-ended trajectories were observed, featuring different paths when the laser is turned on and off. Moreover, by adjusting the laser actuation parameters, the arc exhibited motion in various modes, including "walking", "turning", "jumping", and "flipping" (Fig. 4*F* and *SI Appendix,* Fig. *S39*). For tubular *(SI Appendix,* Figs. S40 and S41*)* and single-helix robots (*SI Appendix,* Fig. S42), they displayed rotational motions (*SI Appendix*, note 9). These results demonstrate that nonreciprocal deformation offers diverse strategies for microscopic robots to achieve directional locomotion on complex terrestrial surfaces. In contrast, VO_2 microrobots that depend on reciprocal deformation exhibit random motion, consistent with theoretical predictions (*SI Appendix,* Fig. S43).

Designing Complex, Nature-Inspired Microrobots Based Nonreciprocal Deformation. By implementing the designed nonreciprocal deformation into complex structures, we can realize a diverse range of 3D robots with additional flexibility. Here, we present a 3D microscopic robot inspired by human bipedal walking. Similar as humans alternate stepping with their legs to achieve linear motion, we designed two helices with opposite chirality as the "legs" of the robot. Each "leg" structure undergoes nonreciprocal deformation, and by sequentially actuating the two helices, long-distance directional motion of the robot can be achieved (Fig. 5 and Movie S8).

In detail, we refer to the nonreciprocal deformation in the ring structures (Fig. 4 *A–C*) and extend the design to the out-of-plane direction (Fig. 5 *A*, *Left*). We fabricated a structure with two helices in opposite chirality (Fig. 5 *A*, *Right*). We use laser beam to induce nonreciprocal shape morphing of the helix, achieving effective motion of the robot, as shown in Fig. 5*B*. When the laser irradiates a single helical structure (State I), it transits to the "on" state (State II), causing the contact point to lift off the ground and displace; when it reaches the "off" state (State III), the contact point returns to the ground (Fig. 5 *B Insets*). The trajectory exhibits nonreciprocal characteristics. Such deformation can be adjusted by controlling parameters of laser actuation *(SI Appendix,* Fig. S44*)*. We also note that using pulsed lasers in complex

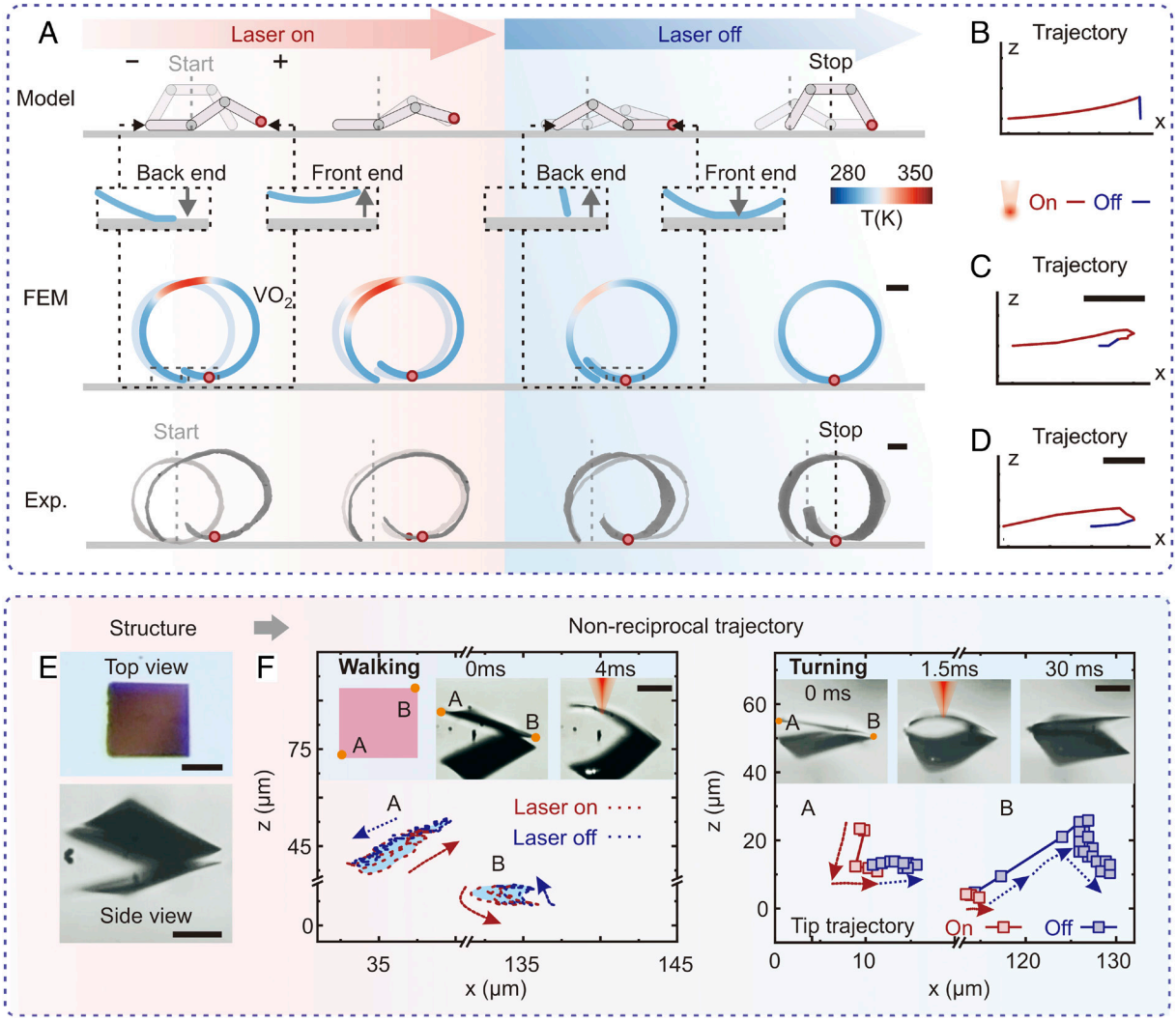

Fig. 4. Directional motion of VO_2 microscopic robots based on nonreciprocal deformation. (*A*) Models, simulations, and experiments of ring-shaped robots with net displacement based on nonreciprocal shape morphing. *Top*, Directional motion of three-link models. *Middle*, The temperature distribution of microrobots during laser-actuated motion, simulated using FEM. Dashed boxes highlight the front and back contact points between the robot and the surface, corresponding to states in the three-link model. *Bottom*, Experimental demonstration of the microrobot achieving directional motion. (*B–D*) Tracked trajectories of the front end contact (red dots) in three-link models (*B*), simulations (*C*), and experiments (*D*). (*E* and *F*) Directional motions of simple square-shaped robots with nonreciprocal tip trajectories. (*E*) Structure of square-shaped robots from the top and side views. (*F*) Nonreciprocal trajectory of square-shaped robots during walking and turning. [Scale bars: 50 μm (*A*), 40 μm (*C* and *D*), 50 μm (*E* and *F*).

structures may lead to uncontrolled motion. To address this, we replace pulsed lasers with a programmable swept-laser strategy, which can achieve the same deformation and controllable motion (*SI Appendix*, note 9 and Figs. S45–S48). Under this driving strategy, independently actuating a single helix generates rotational motion of the microrobot. The states in Fig. 5*C* (State I-III) correspond directly with Fig. 5*B*, and this rotational motion is similar to the rotation of a single helical structure, resembling a human stepping forward on one foot. Inspired by human bipedal alternating movement, we define the laser-actuated helical structure as the "actuated leg" (red square) and the nonactuated helical structure as the "unactuated leg" (indigo square). In Fig. 5*C*, the right-side leg is the actuated leg, moving forward under laser actuation, while the left-side leg is the unactuated leg, passively following the motion. As a result, the entire robot rotates.

Based on this, we can design various actuation sequences for achieving directional forward motions and rotation. When the actuated leg alternates between the left and right, the robot demonstrates forward motion, as shown in Fig. 5*D*, similar as human walking. When we keep actuating the same leg, the robot continues to rotate. For example, when the right-side leg is always actuated, the entire robot rotates clockwise (Fig. 5*E*), while counterclockwise rotation occurs when the left-side leg is actuated. In this experiment, the clockwise and counterclockwise rotation reach approximately 180° within 10 actuations. This microrobot, designed based on human bipedal motion and nonreciprocal deformation, demonstrates a significant degree of in-plane motion freedom. By leveraging our fundamental nonreciprocal deformation principles and a 3D VO_2 thin film platform, complex and customized robot structures can be constructed for various practical applications. All above results show that microscopic robots in various shapes can display unique motion behaviors, and their speed can be controlled by varying laser power, laser frequency, and nanomembrane thickness (*SI Appendix*, note 10 and Figs. S49–S51).

Potential Applications and AI Control Systems for Microscopic Terrestrial Robots. Based on our previously demonstrated microscopic robots, we now further highlight their potential applications and introduce an artificial intelligence control system. By leveraging

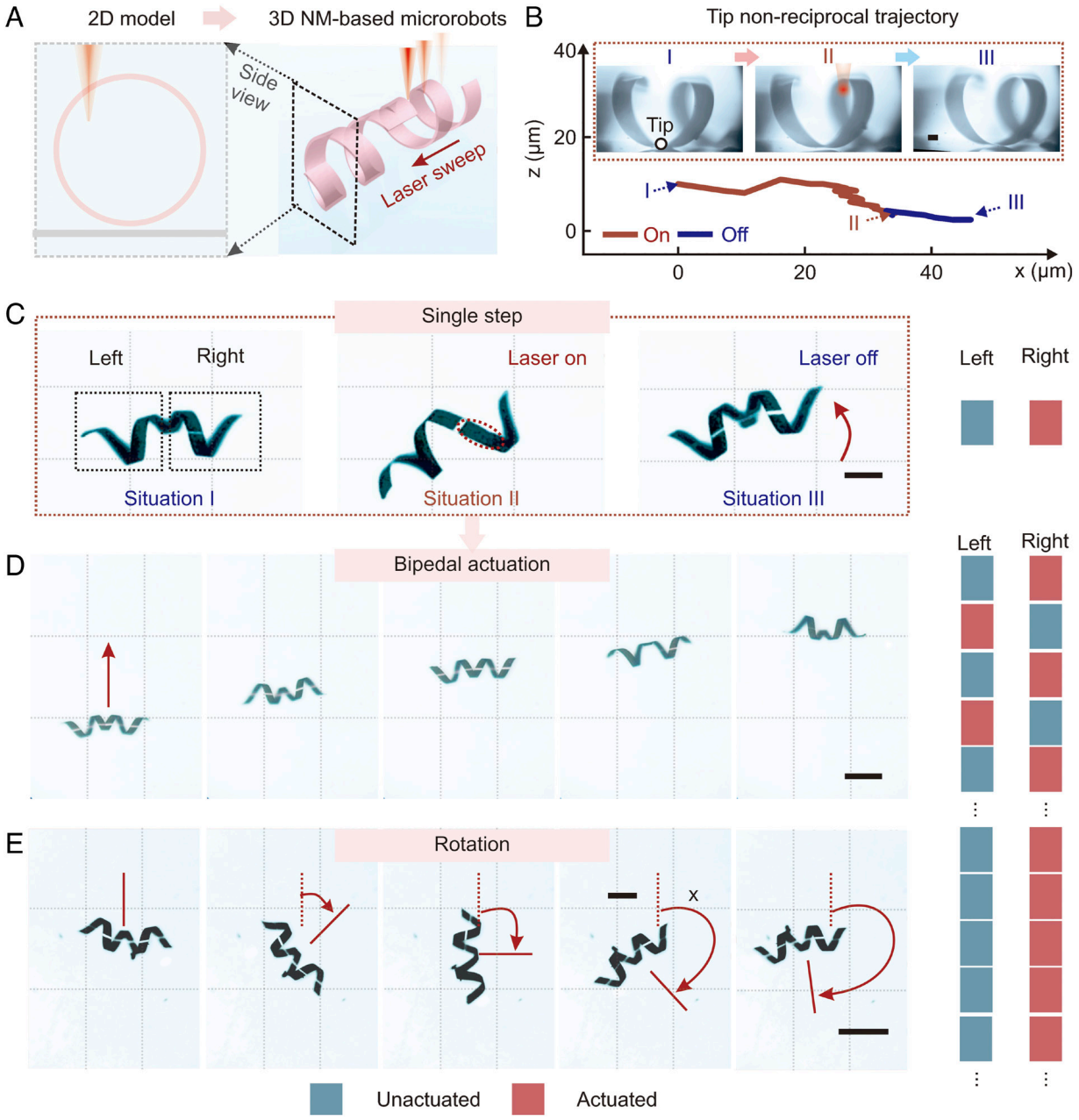

Fig. 5. Design of complex microscopic robots with 3D nanomembranes using a nonreciprocal shape-morphing model. (*A*) *Left*, Schematic of the 2D model for nonreciprocal shape morphing used in Fig. 4. *Right*, Complex robots composed of two helices with opposite chirality, based on VO_2 nanomembranes actuated by sweeping focused laser beams. The side view of the 3D helices is identical to the 2D model on the *Left*. (*B*) Tracked tip trajectories of the robots under laser actuation. The tracked tips are marked in the *Insets*. (*C*) One-step walking of the helical robot, leading to rotation. Blue squares, red squares, and the red arrow represent laser actuation on one leg, passive movement of the other leg, and the walking direction, respectively. (*D*) Long-distance movement of the complex robot by alternatively actuating each leg. (*E*) Rotational movement of the robot by continuously actuating a single leg. [Scale bars, 100 μm (*B*), 400 μm (*C*–*E*)].

their omnidirectional motion, multiple robots can be arranged as individual "pixels" to form user-defined patterns. For example, square-shaped robots can be guided to specific positions to create a Tetris-like pattern (Fig. 6*A*). Throughout the assembly process, the robots can operate without interfering with one another, and the precision of the assembly depends solely on the step size of the robots' movement. This self-assembly could potentially serve display purposes in the future, as our robot structures can be custom-designed, fabricated into large arrays, and simultaneously controlled using the asynchronous actuation strategy based on galvanometer scanners (*SI Appendix*, Fig. S52) and the synchronous actuation strategy based on the digital light processing system (*SI Appendix*, Fig. S53) (45).

Furthermore, by exploiting the characteristic of VO_2 which transitions to a low-resistance metallic phase upon heating, we designed a microcircuit assembly demonstration. Actuated by laser beams, the robot moves toward the two electrodes and spans a ~100 μm gap (Fig. 6 *B*, *Left*). Once in place, global heating induces the VO_2 phase transition, enabling the low-resistance robot to bridge the electrodes and light an LED (Fig. 6 *B*, *Right*). The microrobot can also carry extra electronic components and be scaled down to the submicron dimensions due to CMOS process compatibility and customizable structure, making it suitable for integration with existing integrated circuit systems.

Moreover, in view of the rich design freedom of VO_2 robots, the control strategies for the effective locomotion are influenced by many parameters, such as surface conditions and the shapes of the robots, which are laborious to optimize. We propose an artificial intelligence control system based on RL (46), which

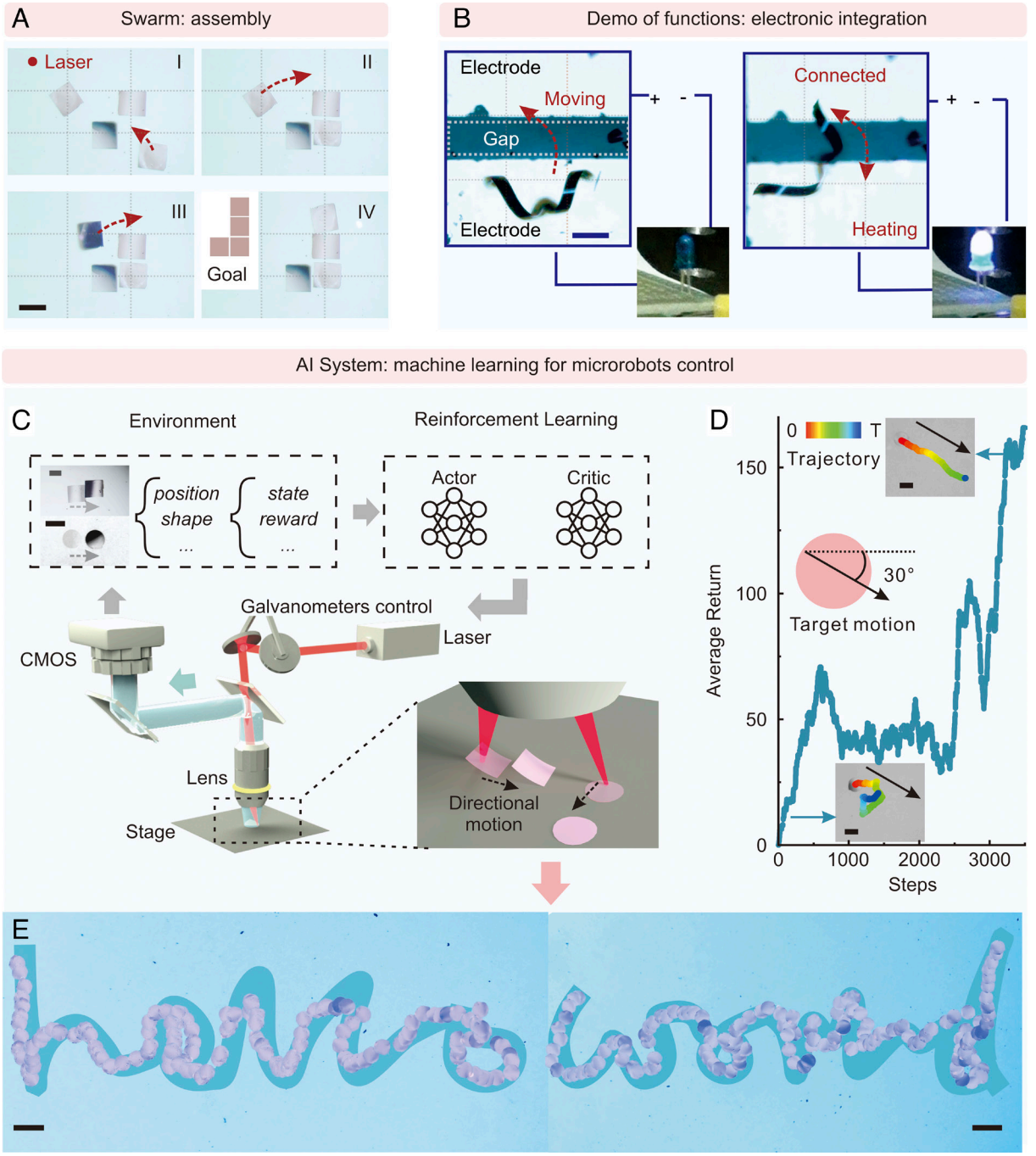

Fig. 6. Assembly, application, and AI control systems for microscopic robots: proof of concept. (*A*) Control of robot swarms for microassembly. (*B*) Demonstration of robot functions, using microscopic robots as electronic components for circuit integration. (*C*) Schematics of the apparatus for controlling the motions of microscopic robots, integrating both software and hardware components. Detailed settings are described in *SI Appendix*, *Microscopic robot control* and note 11. (*D*) Learning progress for a single circular microscopic robot moving toward a target direction. The rolling average of the return over the last 6 epochs is illustrated, with insets indicating the actual trajectory of the robot before learning and after 3,000 learning steps. (*E*) Complex, long-distance "hello world" trajectory motion executed based on policies learned by a reinforcement learning (RL) agent. [Scale bars: 100 μm (*C*), 100 μm (*D*), 200 μm (*E*)].

automatically optimizes the actuation (Fig. 6*C*). The control system trains microrobots to achieve directional movement through the following cycle: The RL algorithm generates an action to actuate the galvo, and deflecting the laser beam toward specific locations on the robot, inducing the locomotion. A camera detects the robot's status, determining the reward based on its displacement toward the target direction after 20 laser shots. Here, high reward indicates effective movement away from its original position toward the proper direction. The RL algorithm then updates the reward and generates the next action. Throughout the cycle, RL uses the soft-actor-critic (SAC) algorithm (47) to continuously self-learn to achieve higher rewards, ensuring that the well-trained algorithm consistently generates actions that actuate the robot in the desired direction (Details in *SI Appendix*, *Microscopic robot control* and Fig. S54).

We perform the self-learning training on a circular robot as the agent (Fig. 6*D*). The target motion direction is 30° toward the lower right. Initially, the average reward is about 40 and the robot moves randomly because of the arbitrary laser irradiation spots. After about 3,200 training steps, the robot moves in the target direction with the average reward about 150, demonstrating the effectiveness of the training algorithm (Movie S9). This algorithm

is also applicable to robots of various shapes, such as the square-shaped robots and the Coccinellid robots (*SI Appendix*, note 11 and Figs. S54–S58). With the trained agent, the microrobot can autonomously navigate complex trajectories by splitting the motion path. It can move along the strokes of the letter "A", "B", "C", and "D" (*SI Appendix*, Fig. S59 and Movie S10) and the symbolic phrase "hello world" (Fig. 6*E and* Movie S11). The RL algorithm automatically optimizes motion control parameters for microrobots of any shape and in any working environment, making it highly desirable for practical applications.

Discussion

In summary, we achieved microscopic robot with directional locomotion on terrestrial environments. The proposed theory with nonreciprocal shape morphing is versatile and critical for achieving microscopic terrestrial locomotion, suitable for a wide range of robot with feature sizes from micrometers to nanometers, where adhesion forces are dominant (22). Such nonreciprocal shape morphing is achieved using materials with hysteresis properties, which can be found in many molecular, metals, oxides, 2D materials, and polymers (48). Except for VO_2 actuated by focused laser, terrestrial microscopic robots can be made from other hysteresis materials and be actuated by different stimuli including magnetic fields, electric fields light, and ultrasound, depending on the material chosen (49). Additionally, the on-demand design of microrobots and their effective locomotion based on AI control provide a versatile platform that promotes potential applications ranging from laboratories to factories. For example, terrestrial microrobots may be new mobile tools for microscopic sensing and manipulations, such as lab-on-a-chip technology, environmental exploration (50), microelectronics, and nanophotonic (17). Terrestrial microrobots can also facilitate the development of distributed wireless microdevices (51) with the ability to navigate in complex terrains, and AI control algorithm may be an effective strategy for such unstructured surface condition.

Materials and Methods

Growth of VO_2 Nanomembranes. VO_2 nanomembranes are deposited by direct current magnetron sputtering (PVD75, Kurt J. Lesker). First, commercial thermal oxide silicon wafers (oxide layer thickness: 100 nm) were ultrasonically cleaned in ethanol (99.7%), acetone (99.5%), and deionized water for 10 min, respectively. After cleaning, the wafers were put into the sputtering device. VO_2 nanomembranes were then grown by a target of pure V metal (99.9%) at oxygen-argon gas flux using an oxygen–argon gas flux ratio of 38 sccm to 60 sccm. During nanomembrane deposition, wafers were heated to 500 degrees, sputtering power was maintained at 200 W, and deposition time was 1,800 s.

Sample Fabrication. A schematic of the microscopic robot fabrication process can be found in Fig. 2*D*. First, VO_2 nanomembranes undergo "patterning" process. Specifically, a positive photoresist (AZ-5214, Microchemicals GmbH, Germany) was spin-coated on VO_2 nanomembranes, and patterned photoresist arrays were fabricated by an optical direct writing lithography system (UPG501, Heidelberg Instruments). Patterns were used to etch VO_2 nanomembranes by reactive ion etching (T_2, Trion) and the photoresist was then removed by ultrasonography in acetone for 3 min. The patterned VO_2 nanomembranes then underwent the "release" process. Samples were immersed in 40% hydrofluoric acid (HF) solution at room temperature for 5 min. High selective etching characteristics of HF removed the silicon oxide layer, and VO_2 nanomembranes were lifted off from the substrate. Due to the internal strain gradient in VO_2 nanomembranes before releasing (*SI Appendix*, note 7), the nanomembranes were self-rolled-up into microstructures after release. The VO_2 nanomembranes were then transferred to ethanol and dried with a critical point dryer (CPD030, Leica) to avoid structural collapse. So far, microscopic robots on the chip have been fabricated. Benefiting from customized patterns by lithography, the robot structures are tunable, involving arcs, rings, tubes, and helices (Fig. 2*F*). More details on the control of microstructures are provided in *SI Appendix*, note 8. Massive fabrication of microscopic robots can be easily achieved, resulting from the one-step roll-up of single materials. *SI Appendix*, Fig. S11 illustrates the on-chip arrays of arc and helical structures. All morphologies of VO_2 microstructures were characterized by scanning electron microscopy (SEM; JSM-6701F, JEOL).

Simulation of Microrobots' Shape Morphing. We have developed a workflow to simulate dynamic deformation process of microscopic robots. A simplified version of this workflow, focused on the driving process, is illustrated in *SI Appendix*, Fig. S34*A*. The structure before the laser drive is regarded as the original shape. After being irradiated by the laser, the microstructure is deformed. Given that the relative position of laser irradiation on the microstructure changes, we designed a time-domain-based step that incorporates multiple physics fields, including light, thermal, and solid mechanics. The process of deforming the microstructure until it stabilizes under laser irradiation is simulated through iterative steps. The structure, once driven to a stable state by the laser, is defined as the actuated shape. When the laser is removed, the iteration of the steps is also used to simulate the deformation process, and finally, the microstructure returns to the original shape.

More details of growth and characterization of VO_2 nanomembranes, sample fabrication, friction force microscopy test, and microrobot trajectory simulation appear in the *SI Appendix*. The details of building laser manipulation system, tracking microstructure tips, simulation of microrobots shape-morphing, and microscopic robot control are also in the *SI Appendix*.

Data, Materials, and Software Availability. All study data are included in the article and/or supporting information.

ACKNOWLEDGMENTS. This work is supported by the National Key Technologies R&D Program of China (2022YFA1207000 and 2021YFA0715302), the National Natural Science Foundation of China (62375054 and 52101214), Shanghai Rising-Star Program (24QA2711700), Science and Technology Commission of Shanghai Municipality (24520750200, 24CL2900200, 21YF1401600, and 21ZR1403500), and Shanghai Talent Programs. Part of the experimental work was carried out in Fudan Nanofabrication Laboratory. The computations in this research were performed using the computing for the future at Fudan platform of Fudan University.

Author affiliations: [a]International Institute of Intelligent Nanorobots and Nanosystems & State Key Laboratory of Surface Physics, College of Intelligent Robotics and Advanced Manufacturing, Fudan University, Shanghai 200438, People's Republic of China; [b]Yiwu Research Institute of Fudan University, Zhejiang 322000, People's Republic of China; [c]State Key Laboratory of Materials for Integrated Circuits, Shanghai Institute of Microsystem and Information Technology, Chinese Academy of Sciences, Shanghai 200433, People's Republic of China; and [d]Shanghai Frontiers Science Research Base of Intelligent Optoelectronics and Perception, Institute of Optoelectronics, Fudan University, Shanghai 200438, People's Republic of China

Author contributions: Yang Wang, J.C., and Y.M. designed research; Yang Wang, X.L., C.L., Zhi Zheng, X.D., and Y.M. performed research; Yang Wang, Ziyu Zhang, G.J., T.C., J.C., and Y.M. contributed new reagents/analytic tools; Yang Wang, Yunqi Wang, C.Y., H.Z., Zhi Zheng, G.J., T.C., J.C., and Y.M. analyzed data; and Yang Wang, X.L., C.L., Yunqi Wang, C.Y., H.Z., Zhi Zheng, X.D., Z.T., Z.D., G.H., X.C., E.S., J.C., and Y.M. wrote the paper.

The authors declare no competing interest.

1. A. J. Ijspeert, Biorobotics: Using robots to emulate and investigate agile locomotion. *Science* **346**, 196–203 (2014).
2. W. Pang *et al.*, A soft microrobot with highly deformable 3D actuators for climbing and transitioning complex surfaces. *Proc. Natl. Acad. Sci. U.S.A.* **119**, e2215028119 (2022).
3. M. Han *et al.*, Submillimeter-scale multimaterial terrestrial robots. *Sci. Robot.* **7**, eabn0602 (2022).
4. W. Hu, G. Lum, M. Mastrangeli, M. Sitti, Small-scale soft-bodied robot with multimodal locomotion. *Nature* **554**, 81–85 (2018).
5. G. L. Wagner, E. Lauga, Crawling scallop: Friction-based locomotion with one degree of freedom. *J. Theor. Biol.* **324**, 42–51 (2013).
6. D. Hu, J. Nirody, T. Scott, M. Shelley, The mechanics of slithering locomotion. *Proc. Natl Acad. Sci. USA* **106**, 10081–10085 (2009).

7. R. Baines *et al.*, Multi-environment robotic transitions through adaptive morphogenesis. *Nature* **610**, 283–289 (2022).
8. B. Gamus, L. Salem, A. D. Gat, Y. Or, Understanding inchworm crawling for soft-robotics. *IEEE Robot. Autom. Lett.* **5**, 1397–1404 (2020).
9. W. Gilpin, M. S. Bull, M. Prakash, The multiscale physics of cilia and flagella. *Nat. Rev. Phys.* **2**, 74–88 (2020).
10. E. M. Purcell, Life at low Reynolds number. *Am. J. Phys.* **45**, 3 (1997).
11. S. Borsley, D. A. Leigh, B. M. W. Roberts, Chemical fuels for molecular machinery. *Nat. Chem.* **14**, 728–738 (2022).
12. H. Xu *et al.*, 3D nanofabricated soft microrobots with super-compliant picoforce springs as onboard sensors and actuators. *Nat. Nanotechnol.* **19**, 494–503 (2024).
13. J. Cui *et al.*, Nanomagnetic encoding of shape-morphing micromachines. *Nature* **575**, 164–168 (2019).
14. B. J. Nelson, P. Salvador, Delivering drugs with microrobots. *Science* **382**, 1120–1122 (2023).
15. M. Z. Miskin *et al.*, Electronically integrated, mass-manufactured, microscopic robots. *Nature* **584**, 557–561 (2020).
16. Q. Liu *et al.*, Micrometer-sized electrically programmable shape-memory actuators for low-power microrobotics. *Sci. Robot.* **6**, eabe6663 (2021).
17. C. L. Smart *et al.*, Magnetically programmed diffractive robotics. *Science* **386**, 1031–1037 (2024).
18. Z. Yan *et al.*, Three-dimensional mesostructures as high-temperature growth templates, electronic cellular scaffolds, and self-propelled microrobots. *Proc. Natl. Acad. Sci. U.S.A.* **114**, E9455–E9464 (2017).
19. H. Han *et al.*, Imaging-guided bioresorbable acoustic hydrogel microrobots. *Sci. Robot.* **9**, eadp3593 (2024).
20. Z. Li *et al.*, Biohybrid microrobots regulate colonic cytokines and the epithelium barrier in inflammatory bowel disease. *Sci. Robot.* **9**, eadl2007 (2024).
21. J. Wang *et al.*, Intelligent micro-/nanorobots for cancer theragnostic. *Adv. Mater.* **34**, 2201051 (2022).
22. R. S. Fearing, Survey of sticking effects for micro parts handling. *J. Int. Confer. Intell. Rob. and Sys.* **2**, 212–217 (1995).
23. A. Aymard, E. Delplanque, D. Dalmas, J. Scheibert, Designing metainterfaces with specified friction laws. *Science* **383**, 200–204 (2024).
24. R. Álvarez-Asencio, J. Pan, E. Thormann, M. W. Rutland, Tribological properties mapping: Local variation in friction coefficient and adhesion. *Tribol. Lett.* **50**, 387–395 (2013).
25. H. A. Miezes, Surface roughness and partical adhesion. *J. Adhesion* **51**, 155–165 (1995).
26. H. T. Tramsen *et al.*, Inversion of friction anisotropy in a bio-inspired asymmetrically structured surface. *J. R. Soc. Interface* **15**, 20170629 (2018).
27. Z. Gu *et al.*, Autonomous nanorobots with powerful thrust under dry solid-contact conditions by photothermal shock. *Nat. Commun.* **14**, 7663 (2023).
28. H. Zeng *et al.*, Light-fueled microscopic walkers. *Adv. Mater.* **27**, 3883–3887 (2015).
29. O. J. Sul, M. R. Falvo, R. M. Taylor, S. Washburn, R. Superfine, Thermally actuated untethered impact-driven locomotive microdevices. *App. Phys. Lett.* **89**, 203512 (2006).
30. X. Chen *et al.*, Photoacoustic 2D actuator via femtosecond pulsed laser action on van der Waals interfaces. *Nat. Commun.* **14**, 2135 (2023).
31. G. J. Simpson, M. Persson, L. Grill, Adsorbate motors for unidirectional translation and transport. *Nature* **621**, 82–86 (2023).
32. O. Sul, *Thermally Actuated Mechanical Systems* (The University of North Carolina at Chapel Hill, 2006).
33. A. J. Cortese *et al.*, Microscopic sensors using optical wireless integrated circuits. *Proc. Natl. Acad. Sci. U. S. A.* **117**, 9173–9179 (2020).
34. A. Zylbersztejn, N. F. Mott, Metal-insulator transition in vanadium dioxide. *Phys. Rev. B* **11**, 4383 (1975).
35. K. Liu *et al.*, Powerful, multifunctional torsional micromuscles activated by phase transition. *Adv. Mater.* **26**, 1746–1750 (2014).
36. E. L. Mockford, A new species of Dicopomorpha (Hymenoptera: Mymaridae) with diminutive, apterous males. *Ann. Entomol. Soc. Am.* **90**, 115–120 (1997).
37. C. Pawashe, S. Floyd, M. Sitti, Modeling and experimental characterization of an untethered magnetic micro-robot. *Int. J. Robot. Res.* **28**, 1077–1094 (2009).
38. A. Humeau, M. Piñeirua, J. Crassous, J. Casas, Locomotion of ants walking up slippery slopes of granular materials. *Integr. Organism. Biol.* **1**, obz020 (2019).
39. X. Li *et al.*, Self-rolling of vanadium dioxide nanomembranes for enhanced multi-level solar modulation. *Nat. Commun.* **13**, 7819 (2022).
40. Z. Tian *et al.*, Deterministic self-rolling of ultra-thin nanocrystalline diamond nanomembranes for three-dimensional tubular/helical architecture. *Adv. Mater.* **29**, 1604572 (2017).
41. R. Cabrera, E. Merced, N. Sepúlveda, F. E. Fernández, Dynamics of photothermally driven VO_2-coated microcantilevers. *J. Appl. Phy.* **110**, 094510 (2011).
42. J. K. Atkin *et al.*, Strain and temperature dependence of the insulating phases of VO2 near the metal-insulator transition. *Phys. Rev. B* **85**, 020101 (2012).
43. S. Li *et al.*, Self-regulated non-reciprocal motions in single-material microstructures. *Nature* **605**, 76–83 (2022).
44. A. H. Gelebart *et al.*, Making waves in a photoactive polymer film. *Nature* **546**, 632–636 (2017).
45. P. Stefano *et al.*, Structured light enables biomimetic swimming and versatile locomotion of photoresponsive soft microrobots. *Nat. Mater.* **15**, 647–653 (2016).
46. S. Muiños-Landin, A. Fischer, V. Holubec, F. Cichos, Reinforcement learning with artificial microswimmers. *Sci. Robot.* **6**, eabd9285 (2021).
47. M. R. Behrens, W. C. Ruder, Smart magnetic microrobots learn to swim with deep reinforcement learning. *Adv. Intell. Syst.* **4**, 2200023 (2022).
48. L. L. Que *et al.*, Numerical simulation and experimental research progress of phase change hysteresis: A review. *Ener. Build.* **253**, 111402 (2021).
49. Y. Yin, J. A. Rogers, Introduction: Smart materials. *Chem. Rev.* **122**, 4885–4886 (2022).
50. X. Q. Wang *et al.*, Somatosensory, light-driven, thin-film robots capable of integrated perception and motility. *Adv. Mater.* **32**, 2000351 (2020).
51. B. H. Kim *et al.*, Three-dimensional electronic microfliers inspired by wind-dispersed seeds. *Nature* **597**, 503–510 (2021).